THE SuperTIGER INSTRUMENT: MEASUREMENT OF ELEMENTAL ABUNDANCES OF ULTRA-HEAVY GALACTIC COSMIC RAYS

W. R. Binns[1], R. G. Bose[1], D. L. Braun[1], T. J. Brandt[2], W. M. Daniels[2], P. F. Dowkontt[1], S. P. Fitzsimmons[2],
D. J. Hahne[2], T. Hams[2,6], M. H. Israel[1], J. Klemic[3], A. W. Labrador[3], J. T. Link[2,6], R. A. Mewaldt[3], J. W. Mitchell[2],
P. Moore[1], R. P. Murphy[1], M. A. Olevitch[1], B. F. Rauch[1], K. Sakai[2,6], F. San Sebastian[2], M. Sasaki[2,6], G. E. Simburger[1],
E. C. Stone[3], C. J. Waddington[4], J. E. Ward[1], AND M. E. Wiedenbeck[5]

[1] Washington University, St. Louis, MO 63130, USA; wrb@wustl.edu
[2] NASA/Goddard Space Flight Center, Greenbelt, MD 20771, USA
[3] California Institute of Technology, Pasadena, CA 91125, USA
[4] University of Minnesota, Minneapolis, MN 55455, USA
[5] Jet Propulsion Laboratory, California Institute of Technology, Pasadena, CA 91109, USA
[6] Center for Research and Exploration in Space Science and Technology (CRESST), Greenbelt, MD 20771, USA

ABSTRACT

The SuperTIGER (Super Trans-Iron Galactic Element Recorder) instrument was developed to measure the abundances of galactic cosmic-ray elements from $_{10}$Ne to $_{40}$Zr with individual element resolution and the high statistics needed to test models of cosmic-ray origins. SuperTIGER also makes exploratory measurements of the abundances of elements with $40 < Z \leqslant 60$ and measures the energy spectra of the more abundant elements for $Z \leqslant 30$ from about 0.8 to 10 GeV/nucleon. This instrument is an enlarged and higher resolution version of the earlier TIGER instrument. It was designed to provide the largest geometric acceptance possible and to reach as high an altitude as possible, flying on a standard long-duration 1.11 million m^3 balloon. SuperTIGER was launched from Williams Field, McMurdo Station, Antarctica, on 2012 December 8, and made about 2.7 revolutions around the South Pole in 55 days of flight, returning data on over 50×10^6 cosmic-ray nuclei with $Z \geqslant 10$, including $\sim$1300 with $Z > 29$ and $\sim$60 with $Z > 49$. Here, we describe the instrument, the methods of charge identification employed, the SuperTIGER balloon flight, and the instrument performance.

Key words: cosmic rays – instrumentation: detectors

Online-only material: color figures

1. INTRODUCTION

The SuperTIGER (Super Trans-Iron Galactic Element Recorder) instrument, shown in Figure 1 just preceding its flight in Antarctica, was developed to measure the elemental composition of ultra-heavy galactic cosmic-ray (UHGCR) nuclei with charge (Z) $26 \leqslant Z \leqslant 40$ with high statistical precision and excellent charge resolution, and to make exploratory measurements into the $40 < Z \leqslant 60$ range. A secondary objective was to accurately measure the energy spectra of the more abundant light elements with $12 \leqslant Z \leqslant 30$ over the energy range $\sim$0.8–10 GeV/nucleon. SuperTIGER was flown during the 2012–2013 Austral Summer, returning data on over 50×10^6 galactic cosmic-ray (GCR) nuclei with $Z \geqslant 10$, including $\sim$1300 with $Z > 29$, and $\sim$60 with $Z > 49$ in 55 days at float.

The origin of GCR nuclei is one of the enduring mysteries in astrophysics. Measurements of the elemental and isotopic abundances have been used over the last several decades to constrain and test theories on the origin of cosmic rays. Cassé & Goret (1978) and Meyer (1985) suggested that the source of cosmic rays was the coronae of stars (types F through M). This was based on the observed enrichment of elements with low first ionization potential (FIP) in cosmic rays, that is similar to that observed in particles from the Sun (solar wind and solar energetic particles). According to Schmelz et al. (2012), the fractionation in particles from the Sun "probably results from a separation of ions and neutrals, which takes place between the photosphere and the corona at temperatures of 6000–10,000 K." The coronal material would then be injected into the interplanetary medium by stellar winds or flare events

and later accelerated to cosmic-ray energies by shocks from nearby supernovae. In 1989, a paper by Binns et al. (1989, p. 997), giving the results of the HEAO-3-C3 experiment concluded, "These abundances are consistent with a cosmic-ray source having a composition similar to that of the solar system, but subject to source fractionation correlated with the first ionization potential (FIP) of each element."

However, Epstein (1980) and Bibring & Cesarsky (1981) showed that refractory elements existing in interstellar dust grains should be preferentially accelerated, compared to elements existing primarily in the gas phase, owing to their large mass-to-charge ratio. The relative enrichment of refractory elements should be similar to the FIP enrichment since many low-FIP elements are refractory and most high-FIP elements are volatile. This work was later extended in a pair of papers (Ellison et al. 1997; Meyer et al. 1997) into a detailed model that reached the same conclusion. Additionally, their model predicted that the abundances of the volatile elements relative to iron should be mass dependent, but refractory abundances should be mass independent. Soon after that, Westphal et al. (1998) published measurements of the $Z = 70$–92 charge range from the Trek instrument aboard the Russian space station Mir, which resolved even-Z nuclei in this charge range for the first time. They concluded that the measured relative abundances for $Z = 74$ through 82 were inconsistent with a chromospheric origin, but consistent with an origin in interstellar gas and dust, with refractory elements preferentially accelerated.

More recently, abundances measured by TIGER at GeV/nucleon energies (Rauch et al. 2009), ACE at energies of hundreds of MeV/nucleon (Binns et al. 2013), and CREAM

Figure 1. SuperTIGER instrument.
(A color version of this figure is available in the online journal.)

at TeV/nucleon energies (Ahn et al. 2010), show that refractory elements are enriched by a factor of about four over volatiles. Furthermore, this enrichment is mass dependent with similar slopes for both refractories and volatiles, and the ordering of these element abundances with atomic mass is greatly improved by comparing them to a mix of normal interstellar material (with solar system abundances) and massive star outflow and ejecta (Woosley & Heger 2007), rather than normal interstellar material alone (Rauch et al. 2009; Binns et al. 2013).

The picture that is currently widely accepted is that a large fraction of cosmic rays originate in OB associations. The OB association origin of cosmic rays was first discussed by Montmerle (1979) and Cesarsky & Montmerle (1981). More recently Higdon et al. (1998) and Higdon & Lingenfelter (2003, 2005, 2013) developed this model in more detail. In this picture cosmic-ray nuclei originate primarily within OB associations, concentrations of young, short-lived, massive stars that form superbubbles in the interstellar medium by the combination of their stellar winds and supernova shocks. The accelerators are believed to be supernova shocks, shocks from the winds of the massive precursor stars (Higdon et al. 1998; Higdon & Lingenfelter, 2003, 2005; Parizot et al. 2004), and colliding winds of massive binaries (Reitberger et al. 2014). Cosmic rays are then accelerated from a mixture of old interstellar gas and dust (with solar-system composition; e.g., Lodders 2003), the wind outflow from massive stars (including Wolf-Rayet stars and their precursor phases), and ejecta from core-collapse supernovae (SNII, SNIb,c). The measured composition of cosmic-ray isotopes and elements is consistent with a mix of interstellar material with outflow and ejecta from massive stars (Binns et al. 2005; Rauch et al. 2009), and with refractory elements enhanced by about a factor of four over volatile elements. Prantzos (2012), on the other hand, can not quantitatively account for the measured $^{22}Ne/^{20}Ne$ ratio (Binns et al., 2005) in his model for an OB association origin.

Recent observations by the *Fermi* Large Area Telescope (LAT) (Ackermann et al. 2013) of γ-rays from two core-collapse supernovae, IC443 (a member of the Gem OB-1 association) and W44, have confirmed the long-held theory that hadrons are accelerated to high energies in at least some supernova remnants (SNR). Additionally, distributed high-energy γ-ray emission has been observed, for example, by Fermi from a "cocoon" with morphology coincident with the Cygnus superbubble (Ackermann et al. 2011), by VERITAS within the radio-shell

of SNR G78.2+2 (Aliu et al., 2013), by HESS in the young stellar cluster Westerlund 2 (Aharonian et al. 2007), and by Milagro in the Cygnus region of the galaxy (Abdo et al. 2007). Dermer & Powale (2013) find that 11 of 12 identified γ-ray emitting SNRs are likely from core-collapse supernovae (SNe). Since core-collapse supernovae result from massive stars, and most massive stars exist in OB associations, it is clear that a large fraction of these SNe occur in OB associations. These γ-ray measurements are highly complementary to results from the direct measurement of cosmic rays and strengthen the OB association model of the origin of cosmic rays (Binns 2011).

TIGER flew over Antarctica in 2001 and 2003 and measured the more abundant individual elements up to $_{38}$Sr. The Super-TIGER flight significantly improves the statistics of these nuclei, extends statistically significant measurements up to at least $_{40}$Zr, and samples the $Z = 50$–60 charge range. Sensitive measurements of these rare $Z \geqslant 30$ elements by SuperTIGER will enable us to test the OB association/superbubble origin model in more detail by reducing the error bars and extending the reach in mass range of the refractory and volatile elements to further explore preferential acceleration and its mass dependence for ultra-heavy cosmic-ray nuclei. We will also search for possible enrichments from nucleosynthesis in massive stars (Woosley & Heger 2007).

As mentioned above, SuperTIGER will also measure the energy spectra of the more abundant elements. Heinz and Sunyaev (2002) have shown that nearby microquasars may impose narrow features in the energy spectra of cosmic-ray nuclei in the energy range from $\sim$1–10 GeV/nucleon. The complement of sensors used in SuperTIGER allows us to measure with greater precision than before (Geier et al. 2006) the energy spectra of GCR nuclei up through $_{30}$Zn over the energy range of $\sim$0.8–10 GeV/nucleon (top of the atmosphere energies).

2. THE SUPERTIGER INSTRUMENT

SuperTIGER was designed to maximize the number of $Z \geqslant 30$ nuclei that could be measured in a series of long-duration balloon flights. This required a design that minimized interactions in the instrument and atmosphere by limiting the column density of the instrument, using materials with low interaction cross-sections, and by flying as high as possible for as long as possible. Since long-duration balloon flights in Antarctica are limited by the duration of relatively stable conditions in the high-altitude winds around the continent, SuperTIGER was designed for simple assembly, permitting early launches, and used no consumables. SuperTIGER has the largest geometric acceptance readily achievable for an instrument meeting the weight limits for flight on a standard 1.11 million cubic meter (40 million cubic foot) balloon. The full instrument weight was 1770 kg.

SuperTIGER incorporates a detector suite selected for excellent charge resolution of ultra-heavy galactic cosmic-ray (UHGCR) nuclei, minimal nuclear interactions, minimum weight, and large geometric acceptance. The techniques used to measure charge and energy are identical to those employed by TIGER, but the implementation has been improved. SuperTIGER (as did TIGER) uses plastic scintillators, acrylic Cherenkov counters, and silica–aerogel Cherenkov counters to determine the element species and kinetic energy of incident particles. Scintillating optical fiber hodoscopes at the top and bottom of the detector stack measure the trajectories of particles transiting the instrument for angle corrections and mapping.
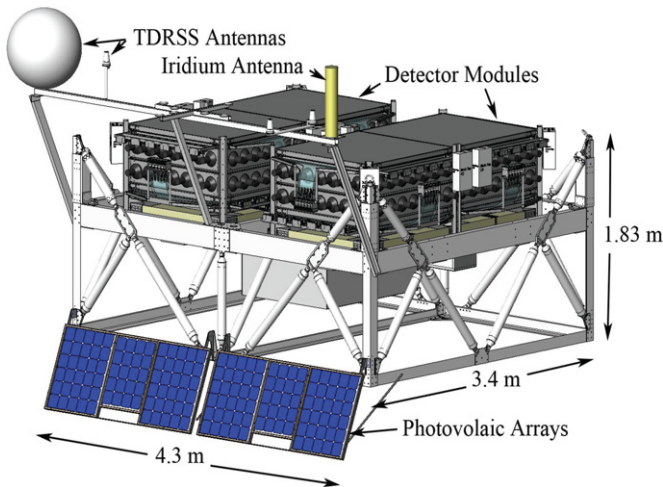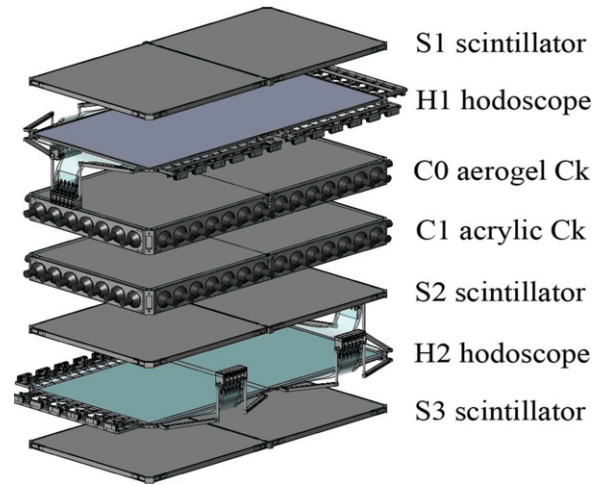
Figure 2. Drawing of SuperTIGER showing the two modules.
(A color version of this figure is available in the online journal.)

Figure 3. Single module shown in expanded view.
(A color version of this figure is available in the online journal.)

For SuperTIGER the scintillator and Cherenkov detector enclosures were floored with an ultra-low-density foam/aluminum-foil composite developed at GSFC, which was also used to support the hodoscope (see Section 4 for details). The tops of the scintillator, Cherenkov, and hodoscope enclosures were thin Al foil. The foam/Al composites and foil windows reduced interactions in the structural materials by ∼20% compared to TIGER. The full geometry factor of both modules combined is ∼8.3 m²sr for particles with trajectory <70° to the zenith. Accounting for interaction losses in the instrument, using $_{34}$Se nuclei as a reference, the calculated "effective" SuperTIGER geometry factor, after interacted particles are removed, is 3.9 m²sr, ∼6.5 times larger than TIGER (0.6 m²sr).

To improve detector performance and add redundancy for enhanced reliability, SuperTIGER is divided into two completely independent modules, as shown in Figure 2. Each module can be mechanically disassembled to a half-module subsystem to enable recovery with any available aircraft in Antarctica including the Basler BT-67 and De Havilland DHC-6 Twin Otter. Each module has an active area of 1.16 m × 2.4 m, approximately the width of TIGER and slightly more than twice as long. Each module has its own electronics systems including trigger, front-end readout electronics, housekeeping sensors, electronic controls, data acquisition/control computer, and data storage. SuperTIGER makes efficient use of the active area by measuring particles that "cross-over" between the active elements of the half-modules. SuperTIGER was designed for "graceful degradation" and to maintain high performance even with the failure of significant numbers of detector channels.

3. MEASUREMENT TECHNIQUES

A SuperTIGER module, shown in expanded view in Figure 3 and fully assembled in Figure 4, consists of three layers of plastic scintillator (S1, S2, and S3), a Cherenkov detector with a silica-aerogel radiator (C0), another with an acrylic radiator (C1), and two scintillating optical fiber hodoscopes (top and bottom) for trajectory determination used to correct for angle of incidence and instrument area response. We measure charge and velocity with combinations of S and C1, or C1 and C0, or S and C0. The S1 and S2 scintillators that make the primary measurements of differential energy loss, dE/dx, are located just above the top hodoscope (H1) and just below the lower Cherenkov (C1)
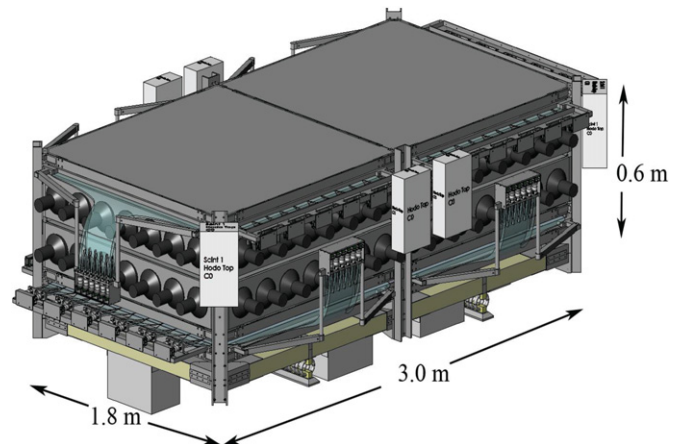

Figure 4. SuperTIGER module.
(A color version of this figure is available in the online journal.)

respectively. The third scintillation counter (S3) is located below the bottom hodoscope (H2), mainly to identify nuclei that have fragmented in the instrument, and is also a backup measurement in case S2 should fail. Placing H2 between S2 and S3 decouples the two scintillators by preventing most δ-rays produced in S2 from reaching S3. However, we have found that we can obtain essentially as good resolution for nuclei with energy below the C0 threshold by ignoring S3 entirely, by simply demanding consistency of S1 and S2 signals.

The use of Cherenkov radiators with different indices of refraction ($n = 1.043$ or 1.025 for C0, and $n = 1.49$ for C1) enables us to use differing techniques to accurately measure charge in complementary energy ranges. For events below the threshold energy of C0, charge is measured by the (dE/dx vs. Cherenkov) technique using the S1 and S2 counters to determine dE/dx with velocity corrections from C1. The use of organic scintillators means that the technique is actually (dL/dx vs. Cherenkov) where L is the light produced by particle energy loss (dE/dx) in the scintillator material. Although $dE/dx \propto Z^2$, L exhibits saturation effects at high specific dE/dx (Birks 1964; Voltz et al 1966; Ahlen et al. 1977; Tarlé et al. 1979; Ahlen 1980; Salamon & Ahlen 1982) and the scintillator response becomes more complicated. An approximation for the charge dependence of the light output is $dL/dx \propto Z^{1.7}$ based
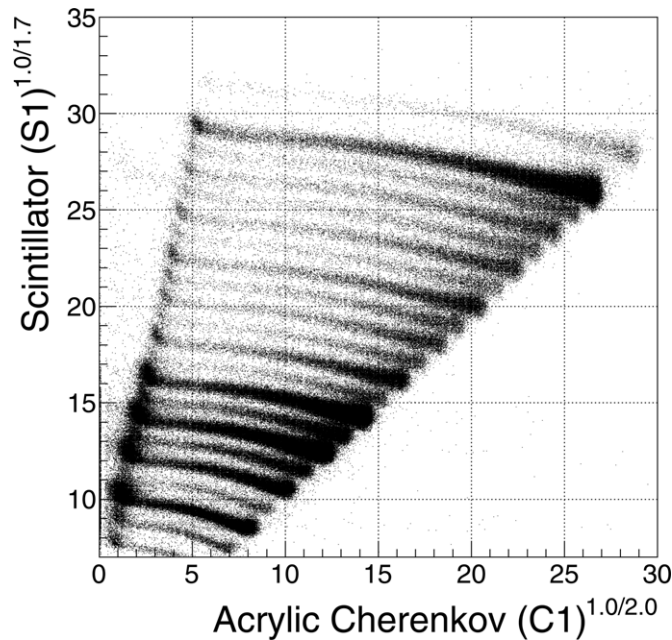
Figure 5. Scatter plot of top scintillator signal $(S1^{1/1.7})$ vs. the acrylic Cherenkov signal $(C1^{1/2})$.

Figure 6. Scatter plot of acrylic Cherenkov signal $(C1^{1/2})$ vs. the aerogel Cherenkov signal $(C0^{1/2}$, refractive index 1.04).

on accelerator calibrations (Binns et al. 1991) and experience from TIGER (Link 2003; Rauch et al. 2009). The SuperTIGER charge separation in this range is shown in Figure 5, which is a scatter plot for a sample of flight data of $S1^{1/1.7}$ vs. $C1^{0.5}$. The charge bands are clearly visible. Full correction for scintillator saturation will use an adaptation of the formulae for dL/dx (in Voltz et al 1966; Tarlé et al. 1979) based on fits to the SuperTIGER data and on a planned calibration at the NASA Space Radiation Laboratory at Brookhaven National Laboratory using fragmented $26 \leqslant Z \leqslant 54$ beams with fragment charge determined using precision solid-state detectors.

For events above the C0 threshold, charge is measured by the [high-n-Cherenkov (C1) vs. low-n-Cherenkov (C0)] technique using the C1 signal, with a small velocity correction from the C0 signal. Above the C0 threshold, the C1 signal depends weakly on particle velocity. The Cherenkov signals have pure Z^2 dependence and do not suffer saturation effects. The high energy data from SuperTIGER are shown in Figure 6 as a scatter plot of $C1^{0.5}$ versus $C0^{0.5}$. Again, the charge bands are clearly visible. The [S vs. C0] analysis also provides useful charge separation, although resolution is inferior to [C1 vs. C0]. The final charge determination is made using a weighted average of the two.

4. THE INSTRUMENT

Details of the SuperTIGER instrument and payload systems are given below.

4.1. Scintillation Detectors:

The scintillators (S-counters) provided both dL/dx measurements and the event trigger. Each S-counter uses two sheets of 1.162 m × 1.162 m × 1 cm ELJEN Technology EJ-208B plastic scintillator mounted side by side in a plane (Figure 3). This scintillator was chosen for its long attenuation length. The scintillation light produced by a nucleus traversing the detector is peaked at about 435 nm. This light is transmitted to the edges of each sheet by total internal reflection and is coupled through a thin air gap to four 1.25 cm square × 1 m EJ-280 wavelength-
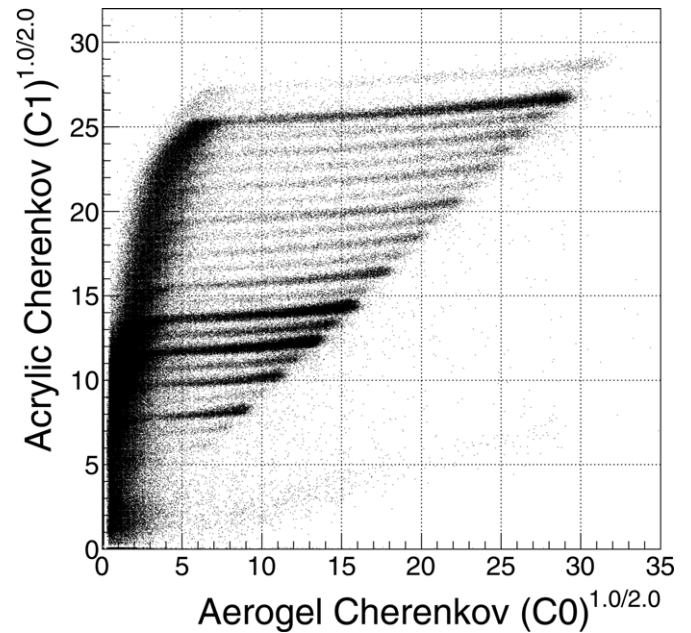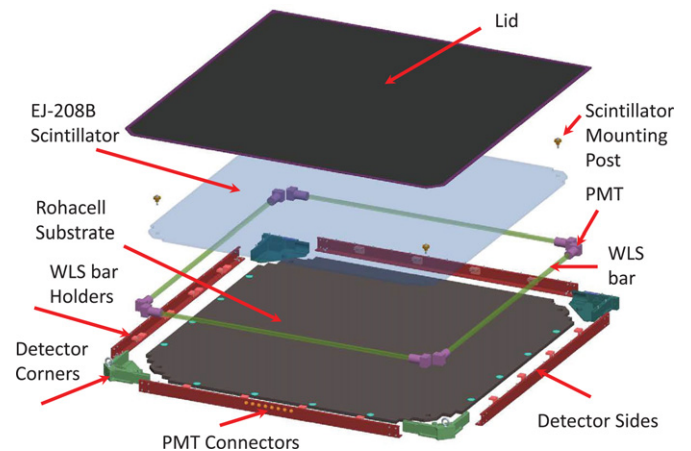
Figure 7. Expanded view of scintillator half-module unit.
(A color version of this figure is available in the online journal.)

shifter (WLS) bars around its perimeter. The WLS bars shift the blue light into the green (peaked at 490 nm); that light is transmitted by total-internal-reflection to Hamamatsu R1924A 2.54 cm diameter photomultiplier tubes (PMTs) coupled to both ends of the WLS bars using EJ-500 optical epoxy. The size of the WLS bars plus structure result in a 6.4 cm gap between the active parts of the side-by-side radiators. A half-detector assembly is shown expanded in Figure 7.

The scintillators were the largest sheets available with the required uniformity. The thicknesses of the scintillators were measured at the factory using an ultrasonic gauge on an 8 × 8 grid (15 cm spacing). The flight scintillators were chosen to have <0.5%/cm thickness gradient over more than 90% of the area with mean gradient <0.25%/cm and maximum gradient <1.0%/cm.

Each scintillator layer within a module was composed of two entirely independent light-tight enclosures with custom extruded Al channel sides and machined corners floored with ultra-low density foam/Al composite sandwich. The foam used for

the floors was Rohacell™ 31-IG (density 0.032 g cm⁻¹), and the top and bottom face sheets of the sandwich were 0.11 mm thick aluminum foil. The thickness of the Rohacell/Al foil sandwich was 1.27 cm. The floor of each enclosure is epoxied to the sides and corners to form a single, mechanically stable, light-tight unit. The enclosure tops are epoxied to 3 mm thick water-cut Al frames outside the field-of-view and sealed to the enclosures with light-tight custom 1.5 mm thick silicone rubber gaskets. The scintillators sit on thin layers of Depron foam, centering them on the WLS bars. Sheets of highly reflective front-surface-aluminized Mylar (thickness 0.05 mm) above and below the scintillators decouple the internal reflection surfaces from the foam and improve light collection and signal uniformity.

The PMT bases used positive high voltage (HV) and radically tapered voltage dividers (relative voltage ratios of: K-D1 1, D1-D2 0.17, D2-D3 0.17, D3-D4 0.24, D4-D5 0.24, D5-D6 0.34, D6-D7 0.34, D7-D8 0.5, D8-D9 0.67, D9-D10 1.0, D10-HV 1.0). This gave nearly linear response to signals as large as 2×10^5 photoelectrons (pe) and an effective dynamic range of 2×10^4 to cover the charge range $10 \leqslant Z \leqslant 60$, including the variations in light reaching each PMT due to particle incident position and angle. Typical flight high voltage was 650–800 V. The bases incorporated charge-sensitive preamplifiers to eliminate pick-up noise that might reduce the resolution of the measurement. The PMTs were wrapped with a single 0.1 mm thick layer of mu-metal foil to cancel the effects of Earth's magnetic field which vary with instrument location and orientation.

As in TIGER, the PMTs were mounted using a compliant RTV to dissipate vibration during transport as well as to allow for thermal expansion/contraction of the WLS bars. However, the instrument was exposed to more transport and thermal stress than expected before flight, and during integration and test at Williams Field in Antarctica a number of the 96 S-counter tubes were found to be broken. As a result, we replaced the module-2 S1-counter (top counter) with a spare counter. Nine additional tubes were not functioning and were presumed to also be broken. Because of the difficulty in accessing these nine tubes, we elected to cap those tubes off and launch with 87 functioning tubes. After 18 hr in flight, one additional tube stopped functioning. Of these 10 failed tubes, one was in an S-1 counter, six were in S-2 counters, and three were in S-3 counters. These failures did not significantly impact in-flight performance due to the SuperTIGER design for graceful degradation. The scintillators provided excellent charge resolution below the C0 threshold and ~100% efficient event trigger for $Z \geqslant 10$ nuclei.

4.2. Cherenkov Detectors:

The Cherenkov detectors used light integration volumes lined with 0.25 mm thick, highly reflective GORE™ DRP light-reflective material to collect the Cherenkov light produced by the silica-aerogel (C0) and acrylic (C1) radiators. Each detector is a single optical volume 118 cm × 480 cm × 20 cm. For ease of recovery it is constructed for easy disassembly into half-detectors with dimensions 118 cm × 240 cm × 20 cm. The enclosures were constructed of 20 cm × 5 cm Al box extrusions machined to accept the PMT housings, with machined end and center fittings. The enclosure tops and floors are similar to those used in the scintillators. Additionally, the C0 aerogel was mounted on a Rohacell/Al pallet (Rohacell thickness 0.48 cm and 0.008 cm aluminum face sheets) that rested on the floor. A full Cherenkov detector is shown with one half expanded and the other half assembled in Figure 8.
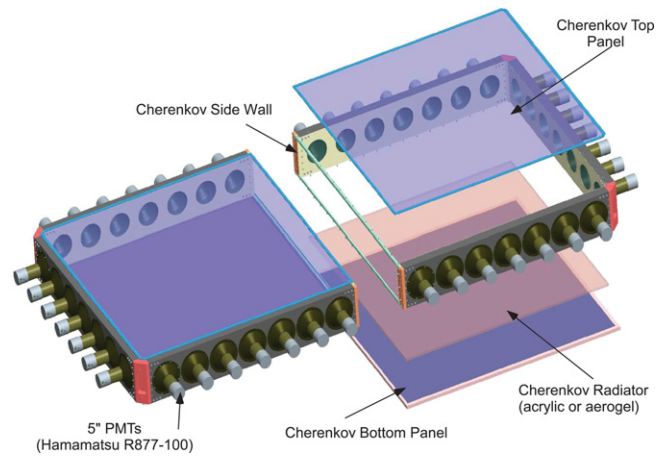
Figure 8. Cherenkov half-detector showing the assembled (left) and expanded (right) module.
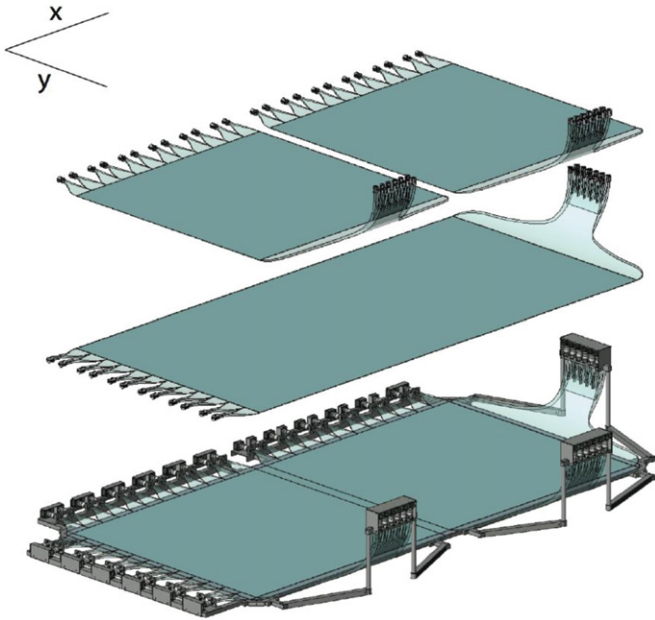(A color version of this figure is available in the online journal.)

Each Cherenkov counter is viewed by 42 12.7 cm Hamamatsu R877–100 PMTs with "Super-Bialkali" photocathodes for high quantum efficiency. These were mounted in custom hydro-formed 0.5 mm thick mu-metal sleeves that served as magnetic shields, mechanical supports, and light covers. Their bases used positive HV with voltage dividers even more radically tapered than those for the scintillators (relative voltage ratios of: K-G 1.0, G-D1 1.0, D1-D2 0.17, D2-D3 0.17, D3-D4 0.33, D4-D5 0.5, D5-D6 0.5, D6-D7 0.75, D7-D8 1.0, D8-D9 1.2, D9-D10 1.5, D10-HV 1.2). These enabled measurements from 10 pe to ~2 × 10^5 pe (dynamic range of 2×10^4) with only 2% nonlinearity in order to span the $10 \leqslant Z \leqslant 60$ charge range. As with the scintillators, the voltage dividers incorporated integrated charge sensitive amplifiers. Flight HV ranged from 950 V to 1200 V.

Each C0 module contained eight aerogel blocks, each approximately 55 cm × 55 cm × 3 cm. Three of the four half-modules contained aerogel blocks with $n = 1.043$ (12 blocks total), while one half-module contained four blocks of index 1.025. These have thresholds of 2.5 GeV/nucleon and 3.3 GeV/nucleon, respectively. The aerogel blocks were purchased from Airglass in Sweden in the early 1990's and were stored in a protective dry-nitrogen environment. To improve light production by eliminating any remaining interstitial alcohol and absorbed aerosol materials, prior to assembly into SuperTIGER they were baked at high temperature in air using a process originally developed for IMAX (Mitchell et al. 1996; Labrador et al. 1993; Labrador 1996). The aerogel blocks are mounted on thin composite pallets covered in GORE™ DRP and held in position by a layer of polyethylene terephthalate, similar to "Saran" Wrap, using a technique adapted from BESS/BESS-Polar (Asaoka et al. 1998).

C1 uses acrylic radiators with bis-MSB wavelength shifter added at a concentration of 25 mg/liter, cast for SuperTIGER by Spartech/Polycast. This material has an index of refraction of 1.49, corresponding to a threshold of 0.3 GeV/nucleon. In each module the radiator consists of two 116 cm × 116 cm × 1.27 cm sheets with a spacing of 4 cm between them. The upper surface of the acrylic radiator was blasted with sodium bicarbonate powder to produce a light diffusing surface and eliminate total internal reflection. The combination of wavelength shifter and diffusing surface greatly improves uniformity of light collection with position.

During SuperTIGER development the signals from various enclosure and PMT configurations and radiators were

Figure 9. Hodoscope detector showing individual fiber planes (top, *x*-layer; middle, *y*-layer) and full assembly (bottom).

(A color version of this figure is available in the online journal.)

simulated using a Geant4 (http://geant4.web.cern.ch/geant4/) Monte Carlo, which uses the measured optical properties of the reflector, PMT quantum efficiency, absorption length, and Rayleigh scattering length in the Cherenkov radiator. These simulations were used to optimize the performance of the light collection efficiency, with the result that the charge resolution for UHGCR, is superior to that of TIGER even though the SuperTIGER detectors are more than twice as large. The numbers of photoelectrons collected corresponded to a mean for singly-charged, minimum ionizing particles of 51 photoelectrons for C1, 10 for C0 ($n = 1.043$), and 5.2 for C0 ($n = 1.025$).

4.3. Hodoscopes:

Figure 9 is a drawing of the scintillating optical fiber hodoscope. Each module has one *x*,*y*-plane on top and one on the bottom. Each plane uses two orthogonal layers of square cross-section scintillating fibers covering a fiducial area of 2.4 m × 1.16 m. The short-axis fibers are 1 mm square in cross-section, with ∼1160 in each layer. Long-axis fibers are 1.4 mm square to provide improved light transmission efficiency over the 2.4 m length, with ∼828 in each layer. The fibers have polystyrene cores and 0.04 mm acrylic cladding. Fluorescent dyes used in the core were butyl-PBD (primary dye) at 1% concentration by mass and dimethyl-POPOP (secondary dye) at 0.02% concentration. Nuclei with $Z = 10$ are expected to give >∼50 pe in a PMT at the greatest distance from the point of incidence along the fiber traversed by the particle. This is based on laboratory measurements of the fibers using a Sr-90 electron source, which show that at the farthest distance of the source from the PMTs we get >∼0.5 p.e.'s. The fibers were drawn over a slowly rotating aluminum wheel, then formed into a ribbon glued together with Arathane 5753 adhesive and cut to length. The fiber fabrication was done in-house at Washington University. The ribbons were laid out to form coordinate layers. The fiber layers were mounted on a Rohacell/Al composite panel with thickness 1.59 cm, with the long layer (*Y* coordinate measurement) glued

to the panel and the short layers (*X* coordinate measurement) glued to the long fibers. The short layer is divided into two subsections separated by 6.0–6.5 cm at the center of the fiber layer to approximately correspond to the separation between the half-module active areas in the scintillators.

The hodoscopes use a coded readout scheme originally developed for TIGER to limit the number of PMTs required (Ward et al. 2011, 2013; Lawrence et al. 1999). The fibers are formatted into "tabs" of 6 (long-axis) or 8 (short-axis) fibers, so the tab width is ∼8 mm. Groups of 12 adjacent tabs at one end of each layer are each viewed by a single Hamamatsu R1924A PMT to give coarse spatial resolution with ∼9.6 cm segments. The tabs on the opposite ends of the fibers are sequentially routed to PMTs so each tab within a coarse group is viewed by a different PMT. This acts as a "vernier" for single-tab localization. A good event has light detected by a PMT at both coarse and fine ends. The root-mean-square uncertainty in position measurement is $\sigma = 8$ mm/$\sqrt{12} = 2.3$ mm. With a separation of 53 cm between top and bottom hodoscope planes, averaged over the effective opening angle of the instrument, for $Z = 40$ the resulting uncertainty in the secant correction contributes only $\sigma_{\mathrm{traj}} = 0.05$ charge units (cu), which is nearly insignificant when added in quadrature with other contributions to obtain the overall charge resolution, σ_Z. The PMT signals are pulse-height analyzed so that large signals from heavy nuclei can be readily distinguished from signals resulting from knock-on electrons or accidental protons traversing the fibers.

Unlike the scintillator and Cherenkov PMTs, a wide linear-output range is not required for the hodoscopes. The PMTs used conventional linear voltage dividers with flight HV ranging from ∼650V to 950V.

To account for variations in fiber number and straightness between fiber tabs, the X–Y positions of the center of each tab on every fiber layer were mapped. Measurements were made approximately every 10 cm along the length of the tab to an accuracy of 0.5 mm. After the fiber layers were glued to the substrate, reference measurements were made to determine the absolute position of the fiber layer relative to the substrate and frame, thereby locating the position of the center of each tab in the instrument coordinate system. These measurements were used to determine the positions where tabs intersect on the perpendicular layers. These positions were recorded as a lookup table allowing the point at which a particle passed through the hodoscope to be quickly determined.

The hodoscope PMT signal for iron nuclei, with trajectory <30° to the vertical, as a function of position along the long-axis fibers is shown in Figure 10. To determine the attenuation length, the x-coordinate was divided into 10 cm bins. Histograms of the hodoscope signals from iron events falling into each bin were made and fit with a Gaussian distribution. The peak channels from the histogram fits are plotted as triangles in Figure 10. Fitting a line to these points gives an attenuation length of ∼1.4 m. The signals falling well below the fitted line are believed to be nuclei that traverse significant thicknesses of the acrylic cladding, which does not scintillate, instead of the scintillating fiber core, or in the case of the drip-lines (e.g., at *x*-coordinates near 200 mm and 650 mm), there may be small gaps between the fibers.

The detection efficiency of the hodoscopes was determined by measuring the fraction of events identified as iron-group nuclei using the S-counters only for which *x*,*y* coordinates were obtained at top and bottom. The average detection efficiency was 96.5%.
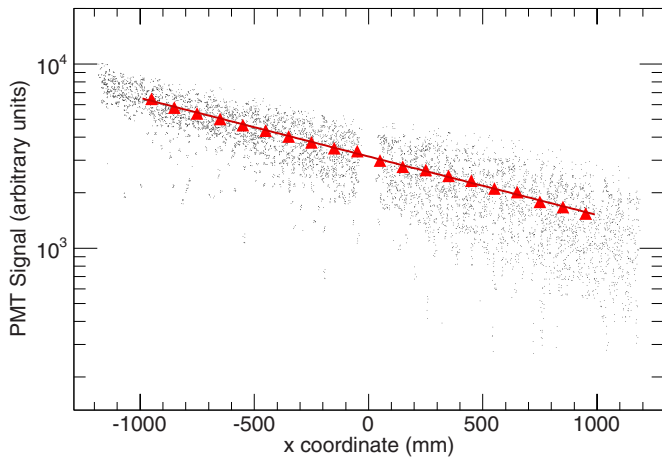
Figure 10. Scatter plot of signal in the scintillating fiber long dimension vs. distance for iron nuclei. The gap in events near the center of the plot is a result of a gap between the two short *x*-fibers.

(A color version of this figure is available in the online journal.)
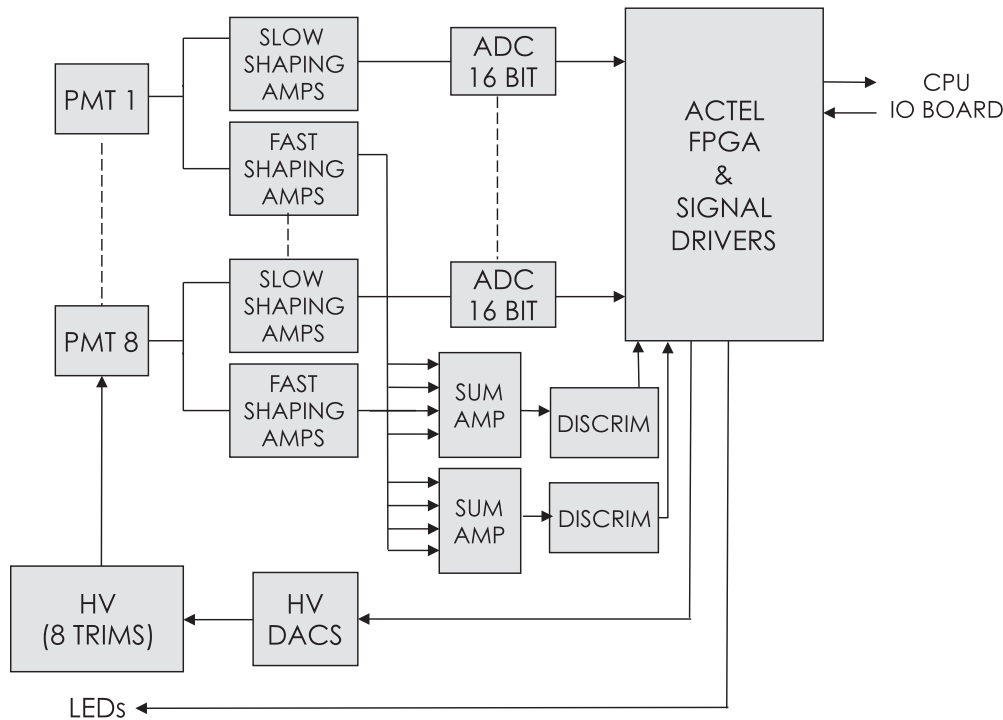
4.4. Electronics:

The trigger and readout electronics for a Front End Electronics (FEE) circuit are shown as a block diagram in Figure 11 (in this case a Scintillator FEE board). As noted above, each of the PMTs in the scintillators and Cherenkov detectors incorporated an integrated charge-sensitive preamplifier. The preamplifiers for the hodoscope detectors were located on the FEE boards themselves. The preamp outputs were fed to shaping amplifiers with time-to-peak of 1 μs and read out by peak sensitive analog-to-digital converters (ADCs). The scintillator and Cherenkov ADCs had 16 bit resolution while the hodoscope ADCs had 14 bit resolution. For the Cherenkov tubes, two gain ranges differing by a factor of 8 were used, each read out by 16 bit ADCs.

The scintillator FEE boards and some of the C1 boards incorporated fast-shaping amplifiers and comparators. Signals registered by the comparators were sent to a field-programmable gate array (FPGA) programmed with the trigger logic. Because the instrument was only intended to be sensitive to particles with $Z \geqslant 10$, the trigger was simple and robust. A logical OR was formed of all the PMT signals from each scintillator layer. The trigger was logically S1 AND (S2 OR S3). Light emitting diodes (LEDs) were used to functionally test the PMT systems on all detectors.

4.5. Data Acquisition and Command:

Each of the two SuperTIGER modules was controlled by its own CPU, each with a root disk and a data disk, both based on Intel 320 series solid state disks (SSD). The data from both CPUs were passed through a multiplexer located on module M1 for telemetry through a TDRSS (Tracking and Data Relay Satellite System) high-gain antenna that could support transmission up to 90 kbps for optimum satellite viewing conditions. A TDRSS omnidirectional antenna, with 5 kbps transmission, and an iridium antenna were also used. On both modules, an S-band transmitter with a downward lobe antenna was used for line-of-sight (LOS) communications up to data rates of 150 kbps, when the balloon was within line-of-sight range of McMurdo. All radio telemetry systems included command uplinks. During the flight, initial tuning of the instrument was performed when LOS communications were available for both uplink and downlink, a period of about 48 hr from the time of launch. After the instrument left LOS range, uplink used primarily the Iridium link. LOS communications were reestablished for a period at the end of the first orbit to increase the downlink rate.

The average event rate during flight for the combined modules was ∼30 events s^{-1}; the size of each telemetered event (both high and low priority) was 398 bytes. The SuperTIGER flight software recorded the full flight data on the SSDs, but used a

Figure 11. Functional block diagram of the scintillator, hodoscope, and Cherenkov readout electronics. Dashed lines indicate additional components of the same kind that are not shown.

compression scheme for telemetered events whereby only the five brightest hodoscope PMTs per side were telemetered (with 12-bit resolution out of 14 available bits; the remaining 2 bits were used to specify the PMT channel number), all Cherenkov PMT signals were sent (with 1 bit out of the available 16 used to specify whether the PMT signal was in the high or low gain channel), while all scintillator PMT signals (16 bit resolution) were telemetered.

All four SSDs failed during flight. Both data disks failed at essentially the same time after 10 days at float (M1 on 19 December at 17:57:47 NZDT and M2 approximately one min later, according to the CPU clocks). After that, they would not accept write commands. The root disks failed approximately 10 days later. Fortunately the CPUs did not need to access their root disks for data acquisition and telemetry to ground or for commanding. Command uplink through iridium and data telemetry through TDRSS proceeded successfully for the full flight duration. Investigation of the SSD failure has not been possible at the time of writing since the instrument has not yet been recovered.

4.6. High-Voltage System:

To maximize the effective dynamic ranges of the detectors and minimize mapping corrections, the high-voltage (HV) system was designed to provide great flexibility in tuning the individual PMT gains. HV power supplies were connected to groups of PMTs through trim boards that allowed each PMT HV to be adjusted over a range of ∼400 V, providing the ability to balance PMT gains. The HV power supplies (HVPS) were compact units from EMCO, supplied potted for vacuum use by the factory. The Cherenkov counters used both 1250 V CA20P and 2000 V CA12P supplies, each serving seven PMTs, and CA12P were used for the S-counters and hodoscope, each serving four scintillator PMTs or six hodoscope PMTs. All connections used shielded Reynolds 600 cable. Scintillator and Cherenkov PMT cables used Reynolds Series 600 connectors while the hodoscope PMT cables were "pig-tails" without connectors. The ends of all cables were potted to resist HV breakdown. Copper mesh over the HVPS and on the top and bottom of the HV trim circuits reduced the local electric field outside the potting to help prevent corona.

The HV systems were tested before flight over a range of temperatures (HVPS −22 to +40 C and PMT bases −30 to +50 C) and at pressures similar to those expected in flight. During flight, one supply had to be turned off due to corona/arcing and five had to be operated at reduced voltage. In addition, a number of EMCO voltage monitors showed significant drift, but the stable responses of the PMTs indicated that this was probably a problem with the voltage monitor signals from the supplies, not a problem with the voltages going to the PMTs. The failure modes indicated that most of the problems were likely due to the EMCO supplies themselves. Although, some hodoscope gains were reduced, the instrument remained fully efficient for $Z \geqslant 22$ particles and geometric acceptance was maintained for the high-priority heavy elements. While light collection in one C0 detector was reduced, the charge determination in the C1 versus C0 range depends only weakly on C0, and there was no significant loss of performance.

4.7. Power System:

The photovoltaic (PV) power system utilizes two strings of 80 SunPower C-60 monocrystalline silicon cells connected in parallel. The cells of each string were connected in series and laminated onto substrates by SunCat Solar. Each 80-cell string consisted of two 5 × 6 cell arrays and one 4 × 5 cell array mounted in the same plane and connected in series. Each contiguous group of 10 cells had a bypass diode installed to protect against cell failure and a blocking diode was placed at the top of each 80 cell array. The two arrays were mounted in a coplanar arrangement on the sun-pointing side of the gondola at an angle of about 70° to the zenith (Figures 1 and 2). The other PV arrays visible in the photograph on the sides and upper part of the gondola, along with those not seen on the other sides of the instrument, powered the balloon electronics and telemetry systems. These balloon systems were the responsibility of the NASA Columbia Scientific Balloon Facility (CSBF).

The charge controller that the PV arrays fed into was a Morningstar TriStar MPPT-45. It was operated in the 24 V mode and charged three pairs of Panasonic LC-X1220P lead acid batteries. The voltage of the PVs measured at the input to the charge controller was very stable at 42 ± 2 V. The system provided ∼240–260 W of power to the instrument throughout the flight. The output of the charge controller was fed into a relay circuit board for each module. Relays could be controlled by discrete commands. Voltages, currents, and temperatures of the power system were monitored. The 24 V main power fed DC–DC converters that provided the lower voltages needed by the FEE boards, high voltage boards, and CPUs.

### 4.8. Gondola, Mechanical Structure, and Thermal Control:

The size of the instrument components and need to minimize weight while satisfying CSBF mechanical requirements and providing protection for the detectors on landing made the gondola especially challenging. Including hodoscope fiber extensions and electronics, each module covers an area of 1.86 m × 3.1 m (Figure 4). Two SuperTIGER detector modules, with spacing between, required a platform size of 4.3 m × 3.4 m. The gondola, shown in Figure 2, uses a light-weight construction with commercial Al C-channels forming the deck and the space-frame elements made of 3 mm wall Al tubing and machined end fittings.

Rigid 7.5 cm thick honeycomb pallets support each module's detector stacks. These were attached to the gondola deck using shock absorbing cable isolators. The detector stacks were built up using six C-channel uprights attached to machined fittings that were bonded to the honeycomb pallets. This design allowed the modules to be fully integrated and tested, including electronics, before final integration with the gondola.

For thermal-vacuum tests at the NASA-Glenn Plum Brook facility (2012 June 26–30), the two modules were stacked one above the other on a mechanical frame, which also supported the modules during shipping to Plum Brook and later to Palestine, TX for final integration with CSBF systems. Parts of this frame were later used in the shipping boxes that carried the modules to Antarctica.

A comprehensive thermal model was developed for Super-TIGER by Scott Cannon at the New Mexico State University Physical Sciences Laboratory, and a passive thermal control strategy was employed using a single box of foam insulation to encase both modules, with 2.54 cm of Techlite insulation on top, 5 cm of Styrofoam insulation on the sides and 2.54 cm of Styrofoam on the bottom. In flight, most temperatures were in the range of −10 to +20°C. However, the top elements of the detector, which had low power dissipation, fell to temperatures
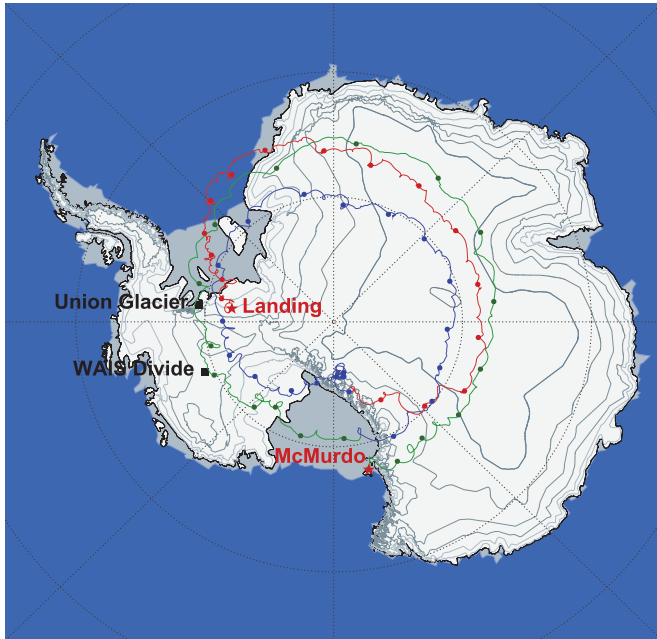
Figure 12. Flight path of SuperTIGER over Antarctica 2012 December 8 to 2013 February 1.

(A color version of this figure is available in the online journal.)

as low as -20°C, somewhat lower than the desired minimum of -10°C. The impact of this on the data was minimal.

5. THE SUPERTIGER FLIGHT

SuperTIGER was launched on 2012 December 8, from Williams Field, Antarctica. In about 2.7 circumnavigations of Antarctica, over the trajectory shown in Figure 12, it flew for more than 55 days at altitudes from about 36.6 km to 39.6 km with an average atmospheric overburden of 4.4 g cm^{-2}. The flight was terminated on 2013 February 1, and set duration records for heavy scientific payloads and for heavy-lift scientific balloons. The instrument returned excellent data on over 50×10^6 cosmic-ray nuclei above the trigger threshold of $\sim Z = 10$. A high-gain TDRSS antenna supported high-rate data downlink, up to 90 kbps depending on satellite view angle. A low-rate ($\sim$5 kbps) TDRSS Omni antenna and an Iridium antenna provided command uplinks and backup data links. The latter was used for most commanding once the instrument was out of line-of-sight (LOS) distance from McMurdo. Good TDRSS links were maintained for most of the flight, with typical transmission rates of 75 kbps. The SuperTIGER priority system assigned high priority to events with signals in the S-counters that exceeded that of vertically incident $Z = 22$ nuclei. The data system transmitted high-priority events first and then filled in with lower priority data. At 75 kbs, essentially all events were transmitted. When poorer links required throttling the transmission to a lower data rate, rates as low as 20 kbs still allowed nearly all high-priority data to be transmitted. Large fractions of lower priority data ($10 \leqslant Z < 22$) were also transmitted. Overall, considering periods with no telemetry and very-low-rate periods, TDRSS data transmission was about 80% efficient for high-priority events, with a smaller efficiency for the very abundant low-priority events, giving the equivalent of 44 days of data recorded for our high-priority data. All triggered events were returned during the two LOS (line-of-sight) periods at the beginning of the flight and the end of the first orbit/beginning of the second.

The flight was terminated on 2013 February 1, due to concerns about increasing instability in the high-altitude winds and safety margins in a CSBF balloon termination battery. Termination was carried out "over-the-horizon" and the instrument landed on the West Antarctic Ice Sheet (WAIS) at 82.24°S 81.91°W, 1625 km from McMurdo and $\sim$600 km from the nearest long-term US camp (WAIS Divide). Although instrument recovery was originally planned for 2014 January, various factors made recovery this year impossible, so the recovery is now planned for the 2014–2015 austral summer.

6. PERFORMANCE

Software that provided housekeeping data displays, scatter plots, and PMT histograms, and which incorporated automated gain and mapping corrections to the signals, was used to tune SuperTIGER after it reached float, by setting HV and thresholds, and for monitoring through a web interface during flight. As a consequence, the basic performance of the instrument was fully verified during the early part of the flight. The methods incorporated in this software have been extended to form the basis for the instrument analysis software, enhanced by additional corrections.

Following flight, the LOS and TDRSS data were reconciled and used to produce a combined data set containing the maximum number of "good" events. Data from the hodoscopes were then used to determine the straight-line trajectory of each event. Pedestal subtraction, PMT gain calibration and adjustments, and corrections for detector position-dependent response (mapping), were applied. The pedestal and gain values are time and temperature dependent, and pedestals were measured every 20 minutes. First order charge determinations were made to identify iron events, and these were accumulated on a 2 cm × 2 cm grid to produce response maps. Corrections were applied to each event for PMT time/temperature dependent gain and incident angle. The exact positions of the detectors in each module were determined with flight data by minimizing the width of the Fe peak.

After initial calibration, the charge (Z) of each particle is determined. The procedure is essentially the same for all techniques and the [S1 vs. C1] process will be used as an example. First, the data are binned by incident angle. Then the iron distribution obtained when plotting $S1^{1/1.7}$ as a function of $C1^{0.5}$ is fit with a quadratic polynomial. (Although dE/dx goes as Z^2, in scintillator the light emitted, dL/dx, goes approximately as $Z^{1.7}$ due to scintillator saturation; Link 2003). The fit is corrected for energy loss through the instrument. For each event, $S1^{1/1.7}$ is scaled by the corrected fit, placing the events on a charge scale with iron at $Z = 26$. The assigned-charge data for all angle bins are combined and residuals in the iron curve as a function of C1 are fit with a quartic polynomial. The charges are corrected using this fit to produce a final charge assignment. All assignments using the scintillators employ a corresponding procedure with fits as a function of either $C1^{0.5}$ or $C0^{0.5}$. In the [C1 vs. C0] technique, the fits are made in $C1^{0.5}$ as a function of $C0^{0.5}$.

The data are analyzed as two separate data sets; events that have a C0 signal above threshold and those that do not have a C0 signal above threshold. Below the C0 threshold, charges are determined separately using [S1 vs. C1] and [S2 vs. C1] as described above. The charge assigned is a weighted average
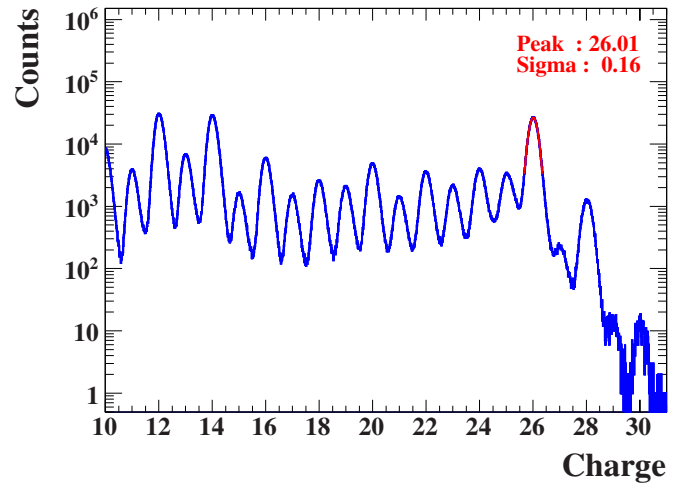
9
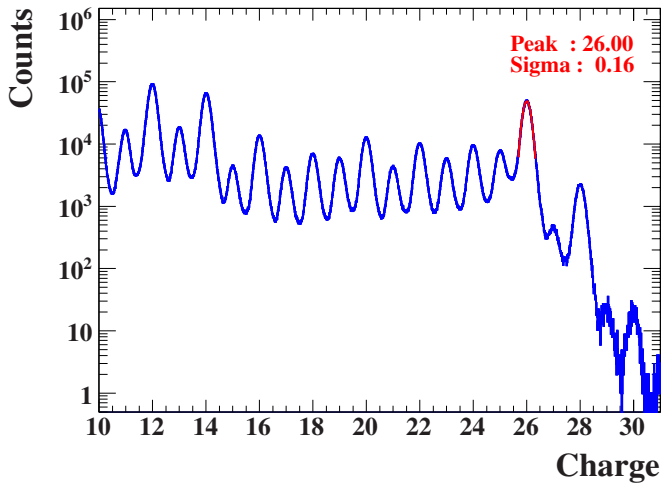
Figure 13. Histogram of events in the energy range below the aerogel Cherenkov threshold (2.5 and 3.3 GeV/nuc for refractive indices (n) = 1.04 and 1.025, respectively). The charge was determined using S1, S2, and C1.

(A color version of this figure is available in the online journal.)

Figure 14. Histogram of events in the energy range above the aerogel Cherenkov threshold (2.5 and 3.3 GeV/nuc for refractive indices (n) = 1.04 and 1.025 respectively). The charge was determined using C1, C0, and S1.

(A color version of this figure is available in the online journal.)

of the two. The resulting charge histogram for $10 \leqslant Z \leqslant 31$ is given in Figure 13. For these data, agreement was required between S1, S2, and S3, but only S1, S2, and C1 were used to determine charge. The Gaussian fit to the Fe peak gives a resolution in charge of $\sigma_Z = 0.16$ cu, demonstrating the excellent performance of SuperTIGER. This compares with the $\sigma_Z = 0.23$ reported by TIGER (Link et al. 2003; Rauch et al. 2009). Note that odd-Z $_{27}$Co and $_{29}$Cu are clearly visible in the histogram even though they are adjacent to the ~100 times more abundant $_{26}$Fe and $_{28}$Ni peaks. Note also the clearly resolved $_{30}$Zn peak.

Above the C0 threshold, charge is determined using a weighted average of [C1 vs. C0] and [S1 vs. C0]. As was the case for the events with C0 signal below threshold, agreement was required between S1, S2, and S3 signals. The resulting charge histogram for $10 \leqslant Z \leqslant 31$ is given in Figure 14. The Gaussian fit to the Fe peak has $\sigma_Z = 0.16$ cu, as was the case for the "below-C0" events. This data set also shows clearly visible $_{27}$Co and $_{29}$Cu peaks and a clearly resolved $_{30}$Zn peak.

The number of iron events in these above- and below-C0 data sets is 2.98×10^6. However, the data set can be expanded to obtain a larger statistical sample for the very rare ultra-heavy nuclei by relaxing the agreement criteria. In this expanded data set (not shown), for the case of events below the C0 threshold, we require agreement between S1 and S2 only (S3 is not used in the analysis at all), and for events above the C0 threshold we require agreement only between S1 and C1 (S2 and S3 are not used in the analysis). This data set contains 3.98×10^6 iron nuclei, with nearly the same charge resolution at iron of about 0.17 cu. For comparison the number of iron events in the combined 2001 and 2003 TIGER flights was 0.56×10^6 (Rauch 2008), giving a factor of 7.1 increase in the number of analyzable events over that of TIGER. The data set also contains 1130 nuclei with $Z > 30.5$ and ~60 nuclei with $Z > 49.5$.

At the present stage of analysis clear peaks can be observed up to $_{44}$Ru (not shown). Work is ongoing to improve the resolution in this charge range, and to extend it up through the $Z = 50$–60 range (with a low statistical sample) through the use of more sophisticated charge and velocity dependent scintillator saturation corrections as discussed in Section 3.

7. CONCLUSION

The SuperTIGER instrument was developed to accurately measure the abundances of ultra-heavy, trans-iron GCR nuclei. It performed well during its record 55-day Antarctic flight, returning data on over 50 million cosmic-ray nuclei. Initial analysis of these data has shown that the charge resolution of the instrument for iron nuclei is 0.16–0.17 charge units at all energies. The numbers of iron nuclei that we have detected is $\sim 4 \times 10^6$, a factor of 7.1 larger than for the combined TIGER flights in 2001 and 2003. Work is ongoing to extend this excellent resolution into the $Z = 50$–60 range.

REFERENCES

Abdo, A. A., Allen, B., Berley, D., et al. 2007, ApJL, 658, L33
Ackermann, M., Ajello, M., Allafort, A., et al. 2011, Sci, 334, 1103
Ackermann, M., Ajello, M., Allafort, A., et al. 2013, Sci, 339, 807
Aharonian, F., Akhperjanian, A. G., Bazer-Bachi, A. R., et al. 2007, A&A, 467, 1075
Ahlen, S. P. 1980, RvMP, 52, 121
Ahlen, S. P., Cartwright, B. G., & Tarle, G. 1977, NIMPR, 147, 321
Ahn, H. S., Allison, P. S., Bagliesi, M. G., et al. 2010, ApJ, 715, 1400
Aliu, E., Archambault, S., Arlen, T., et al. 2013, ApJ, 770, 93
Asaoka, Y., Abe, K., Yoshimura, K., et al. 1998, NIMPA, 416, 236
Bibring, J. P., & Cesarsky, C. J. 1981, in 17th International Cosmic Ray Conf. (Paris), 2, 289
Binns, W. R. 2011, Sci, 334, 1071
Binns, W. R., Christian, E. R., Cummings, A. C., et al. 2013, in 33rd International Cosmic Ray Conf. (Rio de Janeiro), Paper 0646, http://www.cbpf.br/~icrc2013/papers/icrc2013-0646.pdf

Binns, W. R., Crary, D. J., Cummings, J. R., et al. 1991, in 22nd International Cosmic Ray Conf. (Dublin), 2, ed. M. Cawley et al. (Dublin: Reprint), 511

Binns, W. R., Garrard, T. L., Gibner, P. S., et al. 1989, ApJ, 346, 997

Binns, W. R., Wiedenbeck, M. E., Arnould, M., et al. 2005, ApJ, 634, 351

Birks, J. B. 1964, The Theory and Practice of Scintillation Counting (New York: Macmillan)

Cassé, M., & Goret, P. 1978, ApJ, 221, 703

Cesarsky, C. J., & Montmerle, T. M. 1981, in 17th International Cosmic Ray Conf. (Paris), 9, 207

Dermer, C. D., & Powale, G. 2013, A&A, 553, A34

Ellison, D. C., Drury, L. O'C., & Meyer, J. P. 1997, ApJ, 487, 197

Epstein, R. I. 1980, MNRAS, 193, 723

Geier, S., Barbier, L. M., Binns, W. R., et al. 2006, AdSpR, 37, 1955

Heinz, S., & Sunyaev, R. 2002, A&A, 390, 751

Higdon, J. C., Lingenfelter, R. E., & Ramaty, R. 1998, ApJL, 509, L33

Higdon, J. C., & Lingenfelter, R. E. 2003, ApJ, 590, 822

Higdon, J. C., & Lingenfelter, R. E. 2005, ApJ, 628, 738

Higdon, J. C., & Lingenfelter, R. E. 2013, ApJ, 775, 110

Labrador, A. W., Mewaldt, R. A., Schindler, S. M., et al. 1993, in 23rd International Cosmic Ray Conf. (Calgary), ed. R. B. Hicks, D. A. Leahy, & D. Venkatesan (River Edge, NJ: World Scientific), 524

Labrador, A.W. 1996, PhD thesis, Caltech

Lawrence, D. J., Barbier, L. M., Beatty, J. J., et al. 1999, NIMPA, A420, 402

Link, J. T. 2003, PhD thesis, Washington Univ., St. Louis

Link, J. T., Barbier, L. M., Binns, W. R., et al. 2003, in 28th International Cosmic Ray Conf. (Tsukuba), 4, ed. T. Kajita et al. (Tokyo: Universal Academy), 1781

Lodders, K. 2003, ApJ, 591, 1220

Meyer, J.-P. 1985, ApJS, 57, 173

Meyer, J.-P., Drury, L. O'C., & Ellison, D. C. 1997, ApJ, 487, 182

Mitchell, J. W., Barbier, L. M., Christian, E. R., et al. 1996, PRL, 76, 3057

Montmerle, T. 1979, ApJ, 231, 95

Parizot, E., Marcowith, A., van der Swaluw, E., Bykov, A. M., & Tatischeff, V. 2004, A&A, 424, 747

Prantzos, N. 2012, A&A, 538, A80

Rauch, B. F. 2008, PhD thesis, Washington Univ., St. Louis

Rauch, B. F., Link, J. T., Lodders, K., et al. 2009, ApJ, 697, 2083

Reitberger, K., Kissmann, R., Reimer, A., Reimer, O., & Dubus, G. 2014, ApJ, 782, 96

Salamon, M. H., & Ahlen, S. P. 1982, NIMPR, 195, 557

Schmelz, J.T., Reames, D.V., von Steiger, R., & Basu, S. 2012, ApJ, 755, 33

Tarlé, G., Ahlen, S. P., Cartwright, B. G., et al. 1979, ApJ, 230, 607

Voltz, R., Lopes da Silva, J., Laustriat, G., & Coche, A. 1966, JChPh, 45, 3306

Ward, J. E., Binns, W. R., Bose, R. G., et al. 2011, in 32nd International Cosmic Ray Conf. (Beijing), OG1.5, Paper 0714, http://www.ihep.ac.cn/english/conference/icrc2011/paper/proc/v6/v6_0714.pdf

Ward, J. E., Binns, W. R., Bose, R. G., et al. 2013, in 33nd International Cosmic Ray Conf. (Rio de Janeiro), CR-IN, Paper 0869, http://www.cbpf.br/~icrc2013/papers/icrc2013-0869.pdf

Westphal, A. J., Price, P. B., Weaver, B. A., & Afanasiev, G. 1998, Nat, 396, 50

Woosley, S. E., & Heger, A. 2007, PhR, 442, 269